AGU PUBLICATIONS

JGR

Journal of Geophysical Research: Solid Earth

RESEARCH ARTICLE
10.1002/2015JB012047

Key Points:
- Deformation tests were conducted at different effective pressure conditions
- Pore pressure buildup can influence slowness of shear rupture propagation
- Continuous spectrum of slip rate likely exists between fast and slow slips

Supporting Information:
- Figure S1

Correspondence to:
A. Ougier-Simonin,
audreyo@bgs.ac.uk

Citation:
Ougier-Simonin, A., and W. Zhu (2015), Effect of pore pressure buildup on slowness of rupture propagation, *J. Geophys. Res. Solid Earth*, *120*, 7966–7985, doi:10.1002/2015JB012047.

Received 20 MAR 2015
Accepted 5 NOV 2015
Accepted article online 12 NOV 2015
Published online 11 DEC 2015

Effect of pore pressure buildup on slowness of rupture propagation

A. Ougier-Simonin[1,2] and W. Zhu[1]

[1]Department of Geology, University of Maryland, College Park, Maryland, USA, [2]Now at British Geological Survey, Environmental Science Centre, Nottingham, United Kingdom

Abstract Pore fluid pressure is known to play an important role in brittle fracture initiation and propagation, yet the underlying mechanisms remain unclear. We conducted triaxial experiments on saturated porous sandstones to investigate effects of pore pressure buildup on the slowness of shear rupture propagation at different confining pressures. At low to intermediate confinements, rocks fail by brittle faulting, and pore pressure buildup causes a reduction in rock's shear strength but does not induce measurable differences in slip behavior. When the confinement is high enough to prohibit dynamic faulting, rocks fail in the brittle-ductile transitional regime. In the transitional regime, pore pressure buildup promotes slip instability on an otherwise stably sliding fracture. Compared to those observed in the brittle regime, the slip rate, stress drop, and energy dissipated during rupture propagation with concurrent pore pressure buildup in the transitional regime are distinctively different. When decreasing confining pressure instead, the slip behavior resembles the ones of the brittle regime, emphasizing how the observed slowness is related to excess pore pressure beyond the effective pressure phenomenon. Analysis of the mechanical data using existing theoretical models confirms these observations. Quantitative microstructural analyses reveal that increasing pore pressure lessens the dilatancy hardening during failure, thus enhances slip along the localized zone in the transitional regime. Our experimental results suggest that pore pressure buildup induces slow slip in the transitional regime, and slip rates along a shear fracture may vary considerably depending on effective stress states.

1. Introduction

Under an overall compressive loading, rock failure occurs when the shear stress exceeds the rock strength, and failure modes are influenced by overburden pressure, tectonic stresses, interstitial fluids, and temperature. At shallow depths or at low effective pressure (i.e., overburden pressure minus pore pressure) and low temperature conditions, the mode of failure in rocks is brittle; pressure-sensitive inelastic strain induces dilatancy (consequence of the nucleation and propagation of microcracks in rocks) and shear localization [e.g., *Rudnicki and Rice*, 1975]. At high pressure and temperature conditions, thermally activated crystal plasticity processes induce ductile deformation behavior; dilatancy and shear localization are inhibited, instead, deformation tends to be more uniformly distributed (i.e., less localized) [e.g., *Byerlee*, 1968; *Paterson and Wong,* 2005, and references therein]. When the effective confining pressure is sufficiently high, the transition between brittle and ductile failure takes place at low temperatures in porous sandstones [e.g., *Wong et al.*, 1997] as well as in low porosity sedimentary rocks such as anhydrites [*De Paola et al.*, 2009]; the typical stress strain curves are illustrated by *Fisher et al.* [2007]. The mechanisms involved in the brittle-ductile transition depend both on extrinsic variables (stress states, pore pressure, temperature, fluid chemistry, and strain rate) and intrinsic parameters (modal composition of the rock, porosity, crack and dislocation density, etc.) [e.g., *Paterson and Wong,* 2005].

The effective normal stress σ_{eff} exerts important controls on the shear strength and physical properties in rocks [e.g., *Jaeger et al.*, 2007; *Foster et al.,* 2013]:

$$\sigma_{\text{eff}} = \sigma_{\text{n}} - \alpha P_f, \tag{1}$$

where σ_{n} is the normal stress, α is a poroelastic parameter, and P_f is the pore fluid pressure [*Rice and Cleary,* 1976]. For shear strength, α is ~1. Under the law of effective stress, an increase in pore fluid pressure can unclamp a fault by reducing the effective normal stress—hence the frictional resistance to slip, which causes the fault to slip at a lower shear stress. This mechanism is responsible for induced seismicity near fluid injection sites [e.g., *Healy et al.,* 1968; *Keranen et al.*, 2014]. More recently, high-fluid pressure has been

inferred [e.g., *Shelly et al.*, 2006] and measured [e.g., *Saffer and Tobin,* 2011; *Kitajima and Saffer,* 2012] at both the downdip and updip regions in the Nankai subduction zone where nonvolcanic tremor, low to very low frequency earthquakes, episodic tremor, and slip occur. These nonearthquakes like seismic and geodetic events exhibit slower slip rate, smaller stress drops and, in general, lack of high-frequency components, which are referred to as slow slip events here. To date, the role of elevated pore pressure in causing slow slip events is not well understood [e.g., *Obara*, 2002; *Shelly et al.*, 2006].

Deformation experiments under controlled conditions shed lights on the mechanics of faulting and earthquakes. In conventional experiments, pore fluid pressure is kept constant during deformation, either at a value well below (for normal pore pressure) or approaching (for high pore pressure) the confining pressure. In nature, when a fault is stressed to failure, pore fluid pressure is not likely to stay constant as the fault material is compacted and sheared. For instance, frictional heating due to rapid slip during a regular earthquake can raise the temperature within the slip zone [e.g., *De Paola et al.*, 2011], which leads to thermal pressurization of the pore fluid, owing to the discrepancy between the thermal expansion coefficients of the pore fluid and of the solid phase [*Platt et al.*, 2014]. The pore fluid pressure increase induces a reduction of the effective normal stress and consequently enhances shear failure or hydraulic fracturing [e.g., *Sibson*, 1973; *Lachenbruch*, 1980; *Andrews*, 2002].

To investigate the effect of increasing pore pressure on slip behaviors during shear faulting, *Ougier-Simonin and Zhu* [2013] conducted deformation experiments on porous Berea sandstone at both constant and increasing pore pressure conditions. They found that the codeformation pore pressure buildup causes considerable reduction of shear strength in the brittle faulting regime, and it induces slow slip behaviors in the transitional regime where the dynamic propagation of a shear fracture is repressed [*Ougier-Simonin and Zhu,* 2013]. From these experiments, it is unclear whether variation of slip behaviors along faults are discrete, i.e., regular versus slow slips, or there exists a spectrum of intermediate slip behaviors as suggested by *Peng and Gomberg* [2010].

Further, detailed examinations of fault zones show that walls of faults are often bordered by materials that are different from each other and from the more uniform material farther away [*Murrell*, 1977; *Sibson*, 1986, 2003]. The value of the effective stresses may thus vary from point to point within a rock sample or formation [*Murrell*, 1977]. If an increase in pore fluid pressure during failure induces slow slips in the transitional regime [*Ougier-Simonin and Zhu,* 2013], could a decrease in normal stress have a similar effect? Is elevated pore pressure responsible for inducing slow slips or the observed slow slip behavior simply results from effective stress reduction?

With these questions in mind, we expanded the testing conditions of *Ougier-Simonin and Zhu* [2013] to investigate whether the slip behavior varies in a discrete or continuous mode. We included another sandstone with a different porosity to test the generality of the observations. In addition, we conducted experiments with decreasing confining pressure and constant pore pressure to untangle the effects of increasing pore pressure on failure modes and slip behaviors from the effects of normal stress variation. We analyzed the change in the brittleness of rocks at different experimental conditions using the bifurcation model by *Rudnicki and Rice* [1975]. We used the slip-weakening model [e.g., *Rice*, 1980; *Wong*, 1982] to quantify the differences in slip behavior when samples failed in the transitional regime at elevated pore pressure or with decreasing confining pressure. Microscale damage associated to rupture propagation is also analyzed. The microstructural data elucidate the control of the interplay between unstable crack growth and dilatancy hardening over slip behavior in porous sedimentary rocks.

2. Experimental Methods

2.1. Sample Assembly

Laboratory measurements were conducted on Berea and Darley Dale sandstones, with an initial porosity of ~21% and ~14%, respectively. The two rocks have comparable grain size (~0.13 mm and ~0.17 mm, respectively), and both consist of quartz, feldspar, and clay minerals; however, Berea has ~5% of carbonates while Darley Dale has ~3% of mica [*Wong et al.*, 1997]. These sandstones were selected because the high permeabilities (~10^{-13} and ~10^{-14} m^2, respectively) of these rocks ensure that the pore fluid pressure can be fully controlled through an external pressure intensifier during deformation [e.g., *Zhu and Wong,* 1997]. Their mechanical and transport properties are well studied in the brittle faulting, transitional, and cataclastic flow

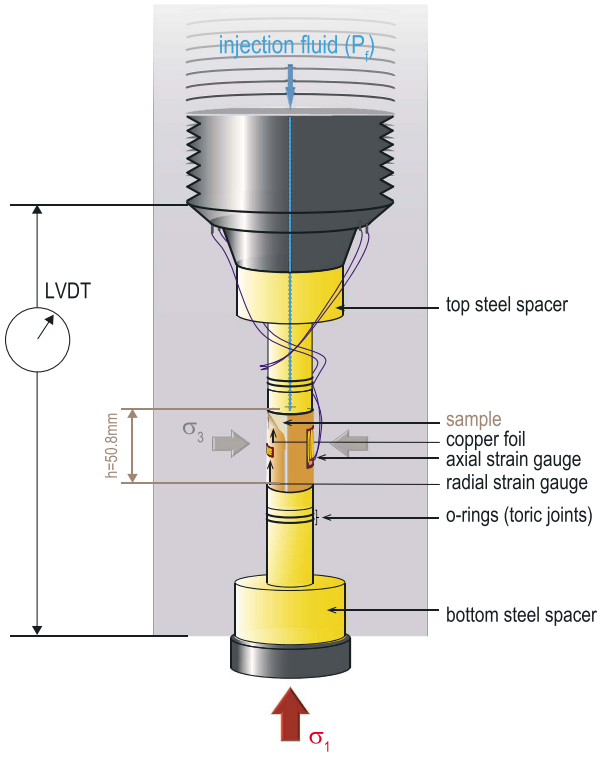

Figure 1. Schematic diagram of the sample setup (not at scale).

regimes [e.g., *Read et al.*, 1995; *Wong et al.*, 1997; *Baud et al.*, 2004]. These rocks undergo the brittle-ductile transition through increasing confining pressures, without elevated temperature [*Wong et al.*, 1997]. The brittle to cataclastic flow transition is expected to occur at a confining pressure of ~70 MPa in Berea sandstone and at ~90 MPa for Darley Dale sandstone [e.g., *Tamarkin et al.*, 2012; *Ougier-Simonin and Zhu*, 2013]. The micromechanisms operative during the transition are primarily frictional sliding and microcracking [e.g., *Menendez et al.*, 1996].

All of the tested samples were cored perpendicular to bedding and ground to a cylindrical shape, with a diameter of 25.4 mm and length of 50.8 mm. Before each test, the sample was saturated with distilled water and jacketed with copper foil of 0.127 mm thick. The jacketed sample was then positioned between two steel spacers, the top one having a concentric hole at the center for fluid access to the pore pressure system (Figure 1). Two Vishay Micro-Measurements (CEA-06-250UW-350) linear strain gauges, one longitudinal (axial) and the other transverse (radial), of 11.43 mm long and 350 Ω electrical resistance were glued in the middle of the sample on the copper foil to record sample axial (ε_a) and radial (ε_r) strains of the deforming sample, respectively (Figure 1). Each strain gauge was used in conjunction with a one fourth Wheatstone bridge. Volumetric strain (ε_v) was subsequently calculated from the measured local strains as $\varepsilon_v = \varepsilon_a + 2\varepsilon_r$; the measured local axial stain was also used for the calculation of the Young's modulus. We note that the strain gauges cover half of sample length and circumference.

2.2. Loading Configuration

All experiments were performed using a triaxial apparatus that allows for axial stress (= maximum principal stress σ_1), confining pressure ($P_c = \sigma_2 = \sigma_3$), and pore fluid pressure (P_f) to be controlled independently. Kerosene and distilled water were used as the confining medium and pore fluid, respectively. A main ram (with a full range 3647 ± 4 MPa) was used to apply axial load, which is recorded by an external load cell. All of the deformation experiments were conducted under drained conditions, at room temperature, with pore fluid pressure fully controlled at desired values. A nominal strain rate of $5 \times 10^{-6}\,s^{-1}$ was applied through the servo-controlled axial displacement (which has a precision of ±0.8 mm), which ensures ample time to maintain equilibration of pore pressure as the rock sample deforms. Axial displacement of the loading piston was measured by a linear variable displacement transducer (LVDT) mounted at the end of the piston outside the pressure vessel and corrected for the effective stiffness (~2×10^8 N/m) of the loading frame. The axial strain data calculated from LVDT measurements agree well with the strain gauge measurements. The rupture propagation in porous rocks is much slower than that observed in low porosity rocks such as granites [e.g., *Lockner et al.*, 1992]. A 16 bit digitizer was used in the data acquisition, and deformation data were recorded at a frequency of 2 Hz (2 data per second), which is adequate to capture the post failure behaviors.

We ran three series of experiments on the two different porous sedimentary rocks at various confining pressures. The first series was performed following the widely used protocol in triaxial deformation studies

Table 1. Summary of Experimental Data[a]

Sample	Confining Pressure P_c (MPa)	Pore Pressure P_f (MPa)	Peak Stress Pks (MPa)	Young's Modulus E (GPa)	Fracture Angle θ (°)	Friction Parameter μ	Dilatancy Factor β at [C';Pks]	Critical Hardening Factor h_c/G
				Berea Sandstones				
B30_iQo	30	10	144.7	21.1	34	0.24	[0.02;0.44]	−0.41
B55_iQo	55	10	186.1	27.5	37	0.17	[−0.05;0.24]	−0.33
B80_iQo	80	10	205.7	23.2	52	−0.14	[−0.24;−0.006]	−0.17
B30_iPf	30	10 to 16.8	127.4	20.0	33	0.26	[−0.15;0.33]	−0.38
B55_iPf	55	10 to 17.9	175.7	22.1	33	0.26	[−0.10;0.45]	−0.41
B80_iPf	80	10 to 18.2	205.2	23.0	38	0.15	[−0.08;0.12]	−0.28
B80_dPc	80 to 69.4	10	203.3	24.5	45	0.21	[0.17;0.14]	−0.31
				Darley Dale Sandstones				
DD30_iQo	30	10	148.3	30.9	37	0.17	[−0.35;0.10]	−0.28
DD55_iQo	55	10	197.3	22.1	39	0.12	[−0.23;0.23]	−0.31
DD80_iQo	80	10	236.0	29.7	45	0.00	[−0.22;0.08]	−0.23
DD30_iPf	30	10 to 16.1	134.1	22.1	35	0.21	[−0.05;0.27]	−0.34
DD55_iPf	55	10 to 20.2	179.1	22.1	35	0.21	[−0.22;0.17]	−0.32
DD80_iPf	80	10 to 21.9	233.6	31.7	35	0.21	[−0.28;0.30]	−0.35
DD80_dPc	80 to 65.4	10	229.7	26.4	37	0.17	[−0.25;0.48]	−0.39

[a]iQo: increasing differential stress Q only; iPf: increasing pore fluid pressure P_f; dPc: decreasing confining pressure P_c. C' is the onset of dilatancy as identified in Figures 2–4 and 6–8.

in which the confining pressure $\sigma_2 = \sigma_3$, and pore fluid pressure P_f were kept constant as the rock sample was stressed to failure due to increasing axial stress σ_1 (iQo tests). The second set was performed at the same stress conditions, but we increased pore pressure after the rock sample was stressed beyond yielding (increasing pore pressure (iPf) tests). The pore pressure buildup during rupture propagation resulted in a

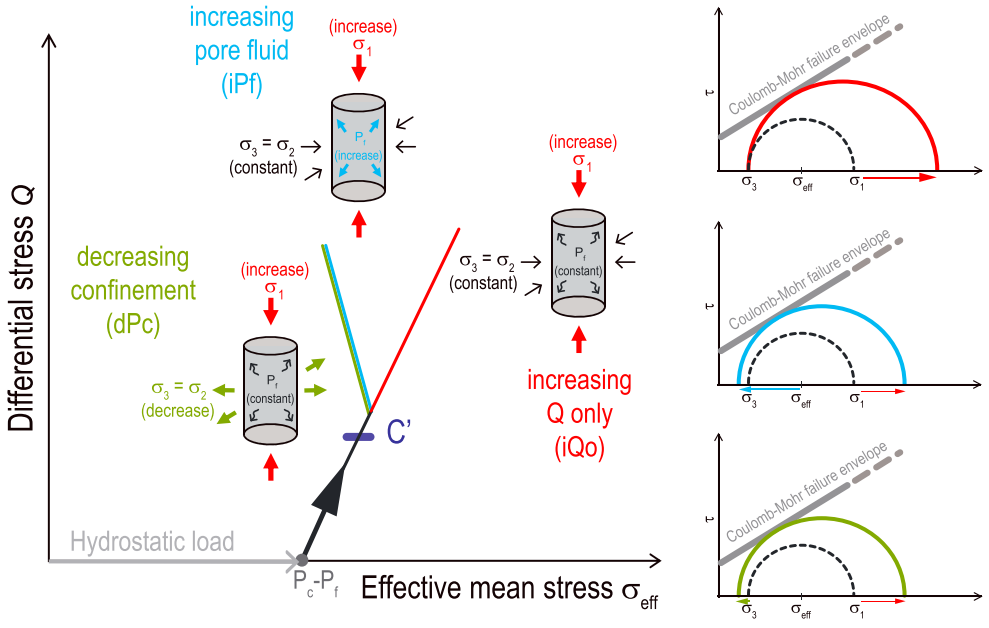

Figure 2. Schematic illustration of the three loading paths. At a preset effective pressure P_c–P_f, a rock sample is deformed through increasing axial load. σ_1, σ_2, and σ_3 are the three principal stresses; P_c and P_f are the confining and pore fluid pressures, respectively. In an iQo test, P_c and P_f are kept constant (red line). In an iPf test, P_f is increased after the onset of dilatancy while P_c is kept constant (blue line). In a dPc test, P_c is decreased after the onset of dilatancy while P_f is kept constant (green line). The iPf and dPc loading paths have identical effective mean stress. The thick arrows represent the changing stress and pressure during deformation; the thin arrows represent stress and pressure that remain constant. Mohr's circles on the right side show how a rock sample is loaded to failure (using the Coulomb-Mohr failure criterion) following the different loading paths.

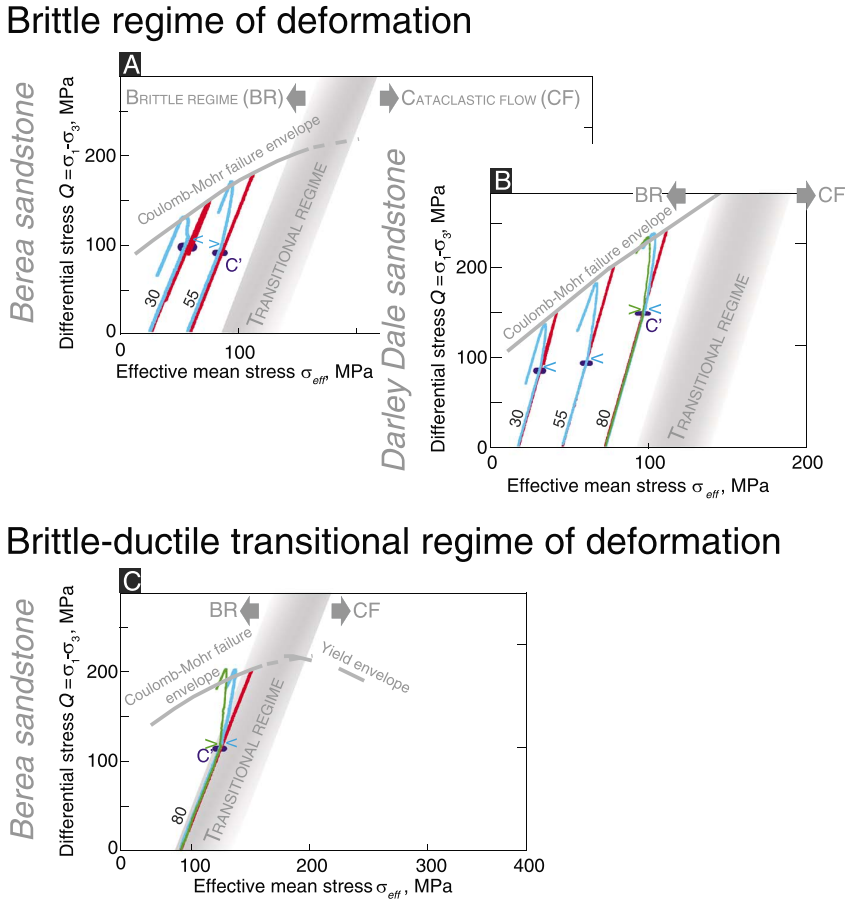

Figure 3. Actual iQo (red), iPf (blue), and dPc (green) loading paths of (a) Berea, (b) Darley Dale sandstone samples failed in the brittle regime, and (c) Berea sandstone samples failed in the transitional regime. Confining pressures P_c = 30, 55, and 80 MPa are indicated. The dark blue short bars mark the onset of dilatancy *C'*. The beginning of pore pressure increase in iPf tests and confining pressure decrease in dPc tests are marked by light blue and green arrowheads, respectively. The Coulomb-Mohr failure envelope for brittle failure (solid) and the yield cap for cataclastic flow (dashed) are based on *Wong et al.* [1997]. The transitional regime between the brittle failure and cataclastic flow is highlighted with a gray band.

lower effective mean stress $\sigma_{eff} = ((\sigma_1 + 2*\sigma_3)/3) - P_f$ in an iPf test, compared to that in a corresponding iQo test [*Ougier-Simonin and Zhu,* 2013]. In the third set, we decreased the confining pressure $\sigma_2 = \sigma_3$ and kept P_f constant beyond yielding (decreasing confining pressure (dPc) tests), so that the effective mean stress in each dPc test is identical to that in the corresponding iPf test (Table 1 and Figure 2).

All samples were first hydrostatically loaded ($\sigma_1 = \sigma_2 = \sigma_3 = P_c$) to a preset effective confining pressure $P_{eff} = P_c - P_f$ (Figure 2). Three confining pressures of 30, 55, and 80 MPa were used in this study such that under these experimental conditions, the sandstone samples failed either in the brittle faulting or transitional regimes (Figure 3). Several tests were repeated at the same conditions to demonstrate the reproducibility of the experimental results (see Figure S1 in the supporting information). Visual inspection of deformed samples retrieved from the pressure vessel indicates localized shear fractures. Except for some Berea samples at low confining pressure of 30 MPa, no audible noise was heard when sample failed.

In an iQo test, i.e., increasing σ_1 with constant P_c and P_f, both the effective mean stress $\sigma_{eff} = ((\sigma_1 + 2*\sigma_3)/3) - P_f$ and the differential stress $Q = \sigma_1 - i_3$ increased simultaneously (red graphs in Figures 2 and 3). In an iPf tests, i.e., increasing σ_1 and P_f (only after yielding) with constant P_c, the initial hydrostatic and deformation loading path were exactly the same as in an iQo test. However, beyond the onset of dilatancy *C'* (where significant inelastic strain accumulation starts), we increased pore pressure with increasing σ_1 as the sample underwent

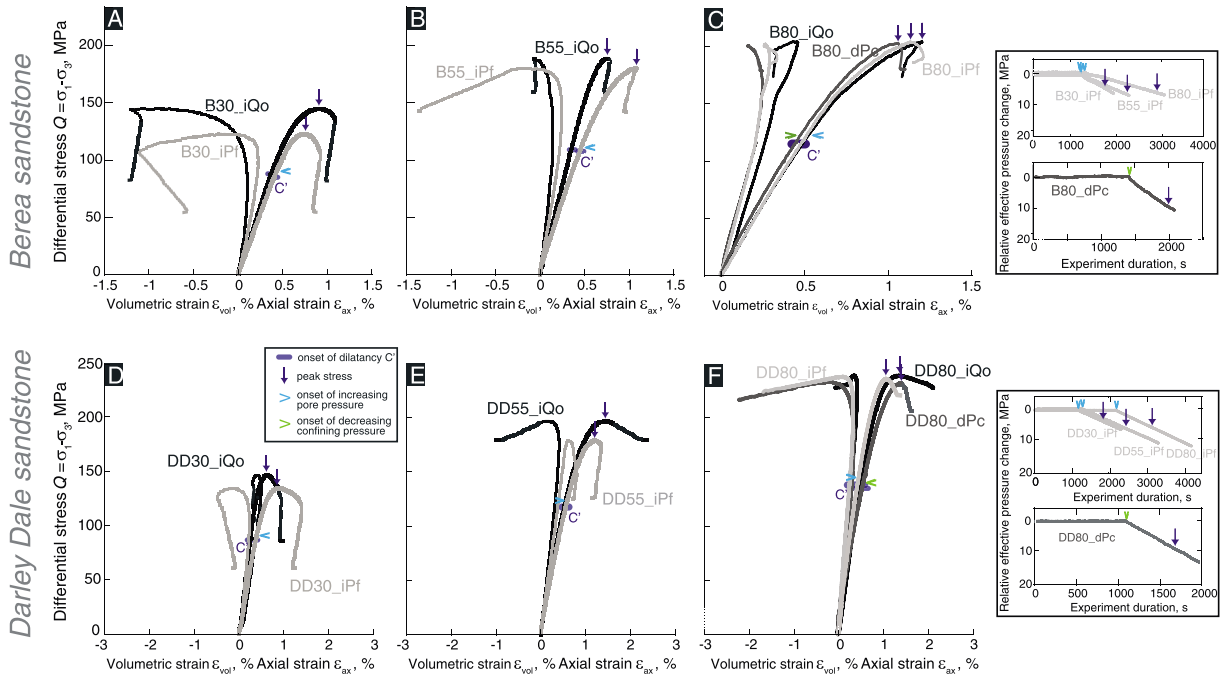

Figure 4. Mechanical data of (a, b, and c) Berea and (d, e, and f) Darley Dale sandstone samples deformed at confining pressures of Figures 4d and 4d 30 MPa, Figures 4b and 4e 55 MPa, and Figures 4c and 4f 80 MPa. Following the geological convention, shortening and compaction of axial strain are positive. The dark blue short bars mark the onset of dilatancy *C'*, and the dark blue arrows mark the peak stress Pks. Beginnings of pore pressure increase and confining pressure decrease are indicated by light blue and green arrowheads, respectively. Postpeak stress failure consists of fault nucleation and frictional sliding. All samples were unloaded shortly after the stress drop levels off. The pore pressure increase and confining pressure decrease recorded in each test is shown in the right graphs. iQo: constant pore fluid pressure, black; iPf: increasing pore fluid pressure, light gray; and dPc: decreasing confining pressure, dark gray.

failure [*Ougier-Simonin and Zhu,* 2013]. This onset of pore pressure increase is marked by blue arrowheads in Figure 3. As a result of such increases in P_f, beyond *C'*, increase in differential stress Q was accompanied by a decrease in effective mean stress σ_{eff} (blue graphs in Figures 2 and 3). In a dPc test, i.e., increasing σ_1 and decreasing P_c (only after yielding) with constant P_f, increase in differential stress Q was accompanied by a decrease in effective mean stress σ_{eff}, equivalent to that in an iPf test (see green graphs in Figures 2 and 3).

The rate of pore pressure increase was kept constant at 4×10^{-5} MPa s^{-1}. At this rate, the nominal strain rates in iPf and iQo tests are comparable, and direct comparison of the deformation behaviors can be made [*Ougier-Simonin and Zhu,* 2013]. This pore pressure increase rate was obtained through a trial and error approach and is expected to vary for different rock types or at different experimental conditions (i.e., strain rate). The pore fluid pressure ranged from 10 to ~22 MPa in our iPf tests (Table 1 and inserts in Figure 4). Comparison of the inelastic behavior and failure mode of samples deformed in iQo and iPf tests allows us to investigate the role of pore fluid pressure in fault propagation. In the dPc tests, the rate of confining pressure decrease was kept constant at 10^{-2} MPa s^{-1} to maintain comparable deformation rate to those in the iPf tests; the confining pressure decreased from 80 to ~65 MPa in these dPc tests (see Table 1 and corresponding inserts in Figure 4). In this study, the dPc tests were conducted at $P_c = 80$ MPa because slow slip behaviors were only observed in the iPf tests at this condition [*Ougier-Simonin and Zhu*, 2013].

3. Results

A total number of 14 experiments are analyzed and shown: among them, mechanical data of four Berea sandstone samples deformed at P_c of 30 and 80 MPa from *Ougier-Simonin and Zhu* [2013] were revised to include sample cross-sectional area corrections. Quantitative microstructural analyses were performed on all 14 deformed samples to understand the mechanisms responsible for different slip behaviors in samples deformed at different conditions.

3.1. Inelastic Behaviors and Failure Modes

Mechanical data of the suite of deformation tests are shown in Figure 4. Following the geological convention, compressive stresses and compactive strains (i.e., shortening and volume decrease) are positive. Tests were stopped as soon as the axial load was clearly identified at a stable value after failure to prevent the jacket's failure. The insert graphs give the relative effective pressure evolution in the samples deformed with increasing pore pressure (iPf tests) and decreasing confining pressure (dPc tests). We note that during and/or at the end of the stress drop observed during the experiments, strain gauges may be compromised by the localized fracture.

At low confining pressure of $P_c = 30$ MPa, both Berea and Darley Dale samples failed in the brittle faulting regime. The mechanical behaviors of the two sandstones are qualitatively similar. As differential stress increases, a linear stress strain relation is observed after the small nonlinear curve caused by the initial crack closure, which indicates the deformation of the samples up to the onset of dilatancy C' is largely linear elastic (Figure 4). Beyond C', pore pressure starts to increase in the iPf tests, with the ongoing axial deformation (Figures 4a and 4d, plus corresponding inserts). Each deformed sample reaches its peak stress—i.e., the highest differential stress that the sample could sustain (marked by dark blue arrows in Figure 4; see Table 1 for exact values) and fails by shear localization accompanied by considerable dilatancy and strain softening (Figure 4). In all four samples, a sudden loss of axial load was observed during deformation. Compared to samples deformed in iQo tests (Figures 4a and 4d), the peak stress of samples under the iPf loading conditions is lower (Table 1 and Figures 4a and 4d), indicating a reduction in brittle strength due to decreasing effective mean stress via pore pressure buildup. This result is consistent with the law of effective stress [e.g., *Scholz*, 2002]. Otherwise, the failure behavior is very similar to that in iQo tests. Note that the maximum pore pressure reached in all iPf tests varies but remains well below the confining pressure P_c (Table 1): up to 16.8 MPa for B30 and 16.1 MPafor DD30, respectively.

At an intermediate confinement $P_c = 55$ MPa, both sandstones exhibit sudden loss of axial load during deformation, indicating that the failure mode is in the brittle regime Figures 3a, 3b, 4b, and 4e). However, compared to samples deformed at $P_c = 30$ MPa, the magnitude of the stress drop is smaller (Figures 4b and 4e). Additionally, the stress drop in DD55_iQo is more gradual (i.e., the slope of the postpeak stress strain curve is less negative) compared to the others deformed at the same or lower effective pressure. The maximum pore pressure reached was up to 17.9 MPa for B55 and 20.2 MPa for DD55, respectively.

At $P_c = 80$ MPa, no sudden loss of axial load was detected while deforming sample B80_iQo under constant pore pressure, indicating that dynamic failure is prohibited at this confinement. Stress strain and microstructural analyses further reveal a small stress drop (Figure 4c), and a deformation band (Figure 5) in B80_iQo, which suggests that the failure mode, is in the transitional regime (i.e., failure is localized but stable). In contrast, at the same confinement, the loss of axial load is detected in sample B80_iPf deformed with increasing pore pressure. Due to the pore pressure buildup during deformation, effective pressure in B80_iPf is ~62.5 MPa at peak stress (down from 70 MPa). The effective pressure change is -8.2 MPa ($P_{eff} = 61.8$ MPa) at the end of the stress drop. Deformed with decreasing confining pressure, a sudden loss of axial load was detected in Berea sample B80_dPc. In fact, the failure behavior in B80_dPc resembles more the brittle faulting at lower confinements than that in B80_iPf. In this test, P_{eff} decreased from 70 MPa to 58.4 MPa at peak stress and to 57.6 MPa at the end of stress drop. The inelastic behaviors and failure modes of Darley Dale sandstone samples deformed at $P_c = 80$ MPa are similar to those deformed at $P_c = 55$ MPa, with even smaller dilatancy and more gradual stress drop, indicating that this confinement is not high enough to prohibit brittle faulting in Darley Dale samples (Figures 4e and 4f). At $P_c = 80$ MPa, the peak stresses for B80_iQo (P_{eff} ~70 MPa), B80_iPf (P_{eff} ~62.5 MPa), and B80_dPc (P_{eff} ~58.4 MPa) are 205.7 MPa, 205.2 MPa, and 203.3 MPa, respectively; the peak stresses for DD80_iQO (P_{eff} ~70 MPa), DD80_iPf (P_{eff} ~63.7 MPa), and DD80_dPc (P_{eff} ~59.7 MP) are 236.0 MPa, 233.6, and 229.7 MPa (Table 1 and Figure 4), consistent with the effective stress law.

3.2. Shear Fracture in Deformed Samples

Quantitative microstructural analyses were conducted to compare stress-induced microcracking in samples deformed at different conditions. Double polished thin sections of 30 μm thick were made for a subset of deformed samples at the end of the test to reveal the macroscopic fault plane subsequently used to determine the fault angle θ (Figure 5). The cut was carefully placed along the longest dimension of the visible

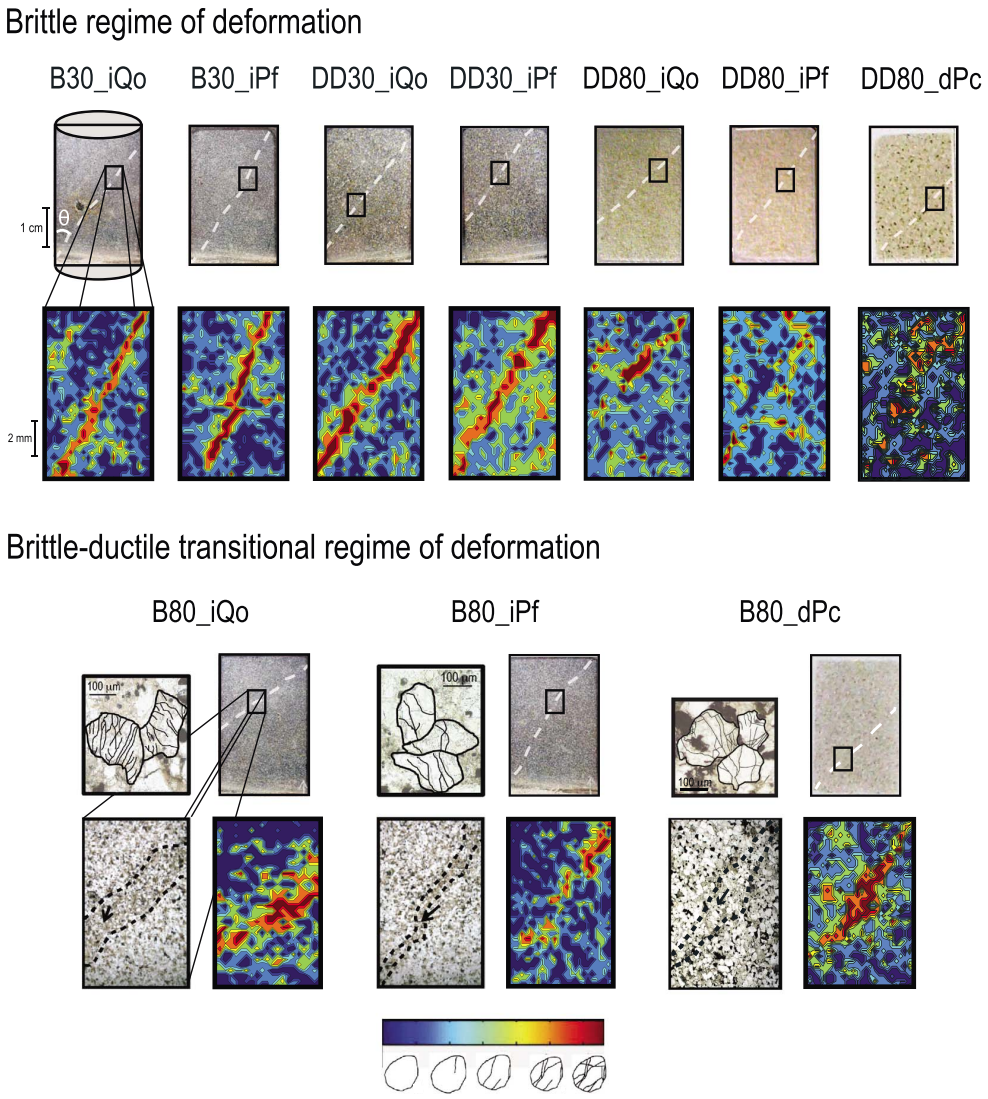

Figure 5. Microstructure of 10 deformed samples. (top) Berea and Darley Dale samples failed in the brittle regime under iQo, iPf, and dPc; (bottom) Berea samples failed in the transitional regime under iQo, iPf, and dPc. Micrographs of Berea samples from *Ougier-Simonin and Zhu* [2013] are included for comparison. Localized shear band (fault plane) is highlighted by a white dashed curve on thin section pictures. Microscale damage index map within the shear band (boxed areas) is shown with the color code on the right; the dark blue represents zero count of microcracks, and colors change from light blue to dark red as microcrack counts increase from 1 to 4 [*Tamarkin et al.,* 2012]. Fracture angle θ is marked to illustrate. To help visualize the stress-induced cracks, high-magnification micrographs (locations are indicated by black arrows) are shown on top of the three Berea samples deformed at $P_c = 80$ MPa.

macroscopic fractures exhibited on the sample surfaces. *Menendez et al.* [1996] developed a damage index for tracking microcrack density in each grain. By assigning different colors to each index value, *Tamarkin et al.* [2012] designed a colored map to illustrate the damage distribution within a deformed sample.

The damage maps show that all samples deformed at $P_c = 30$ MPa developed well localized throughgoing shear fracture of maximum grain crushing (samples B30_iQo, B30_iPf, DD30_iQo, and DD30_iPf in Figure 5) [see also *Ougier-Simonin and Zhu*, 2013, Figure 4]. The fault plane is at ~33 ± 1° with respect to the maximum principal stress σ_1 (Table 1) in Berea sandstones and ~36 ± 1° in Darley Dale. The difference in fault angles between an iPf and a corresponding iQo test is insignificant.

Under the same loading configuration (i.e., iQo or iPf), fault angles of deformed samples increase with increasing confinements. In addition, with increasing confinement, the fault angles of iPf or dPc tests become notably smaller than that in the corresponding iQo tests (Table 1). At $P_c = 80$ MPa, sample B80_iQo exhibits a diffuse zone of damage with an angle of about $53 \pm 1°$ to σ_1 (Figure 5, bottom left), indicating failure in a transitional regime between the brittle faulting and the distributed cataclastic flow. However, at the same confinement, sample B80_iPf shows a more localized damage zone, with an angle of $38 \pm 1°$ (Figure 5, bottom middle). Localized failure is also observed in sample B80_dPc, with an angle of $35 \pm 1°$ (Figure 5, bottom right). The damage index maps show that intense microcracking (i.e., grains with four or more cracks) in B80_iPf is noticeably less compared to that in B80_iQo, as well as in B80_dPc under the same decreasing effective mean stress (Figure 5). Under the iQo loading configuration, Darley Dale sandstone failed in the brittle faulting regime at confinements of 30 to 80 MPa. Damage in all samples appears localized, and fault angles increase with higher confining pressure. Microcrack intensity in sample D80_iPf is lower than that in D80_dPc, consistent with what observed in Berea sandstone.

4. Discussions

4.1. Effect of Pore Pressure on Fault Nucleation

Rudnicki and Rice [1975] developed a constitutive model of where the inception of shear localization is characterized by a friction parameter μ, a dilatancy factor β, and hardening modulus h.

For triaxial compression tests, the friction parameter μ can be obtained through fault angle θ [*Wong et al.*, 1997]:

$$\mu = \frac{2\sqrt{3}\sin\left(\pi/4 - \theta\right)}{3 - \sin(\pi/4 - \theta).} \tag{2}$$

Note that the friction parameter μ defined by *Rudnicki and Rice* [1975] is less than tanϕ, the slope of the Mohr-Coulomb failure criterion in the normal versus shear stress domain. In this study, μ decreases with increasing confinements in iQo tests and remains the same for all iPf tests except B80_iPf (see Table 1). At $P_c = 80$ MPa, μ of B80_iQo is negative, whereas μ of DD80_iQo is zero; increasing pore pressure or decreasing stress during failure results in positive μ with values close to the ones calculated at low P_c (Table 1).

The dilatancy factor β defines the ratio of the plastic strain increments and can be expressed as follows:

$$\beta = -\sqrt{3}\frac{{}^{\Delta}\varepsilon_{v,P}/_{\Delta}\varepsilon_{a,P}}{3 - {}^{\Delta}\varepsilon_{v,P}/_{\Delta}\varepsilon_{a,P}}, \tag{3}$$

with $\Delta\varepsilon_{a,P}$ being the plastic axial strain increment and $\Delta\varepsilon_{v,P}$, the plastic volumetric strain increment [*Rice*, 1975; *Wong et al.*, 1997]. Since the measured strains ε_a and ε_r contain both the elastic and inelastic components (and consequently so does the calculated ε_v), we use the onset of dilatancy *C'* as the bench mark to identify the initiation of plastic deformation. We determine the incremental plastic strains by removing the calculated elastic response from the measured deformation assuming no change in elastic parameters [e.g., *Wong et al.*, 1997; *Makhnenko and Labuz*, 2015]. The resulting plastic shear strain γ_P and the corresponding plastic volumetric strains $\varepsilon_{v,P}$ are as follows:

$$d\varepsilon = -\frac{d\sigma_{\text{eff}}}{K} + d\varepsilon_{v,P}, \qquad d\gamma = \frac{d\tau}{G} + d\gamma_P, \tag{4}$$

where G and K are the elastic shear and bulk moduli, respectively, and τ the shear stress [*Rudnicki and Rice*, 1975]. The range of β values at *C'* and peak stress calculated from Figure 6 are reported in Table 1. At peak stress, the only negative β value is for B80_iQo, consistent with the transitional failure mode where dilatancy is inhibited. In contrast, β values for B80_iPf and B80_dPc are positive, confirming that decreasing effective mean stress promotes dilatant inelastic deformation. From β values alone, no clear difference can be made on the effect of pore pressure buildup versus confinement decrease. In Darley Dale samples, iPf and dPc tests are also generally more dilatant than iQo tests (Figures 6d–6f), though the differences in β values are smaller (Table 1). In both sandstones, at 30 and 55 MPa, β values are comparable between the iQo and iPf tests (Figures 6a, 6b, 6d, and 6e). At 80 MPa, however, β values are noticeably more negative in the iPf tests compared to the correspondent iQo counterparts (Figures 6c and 6f). This suggests that effect of increasing pore pressure on failure is more pronounce in the transitional regime.

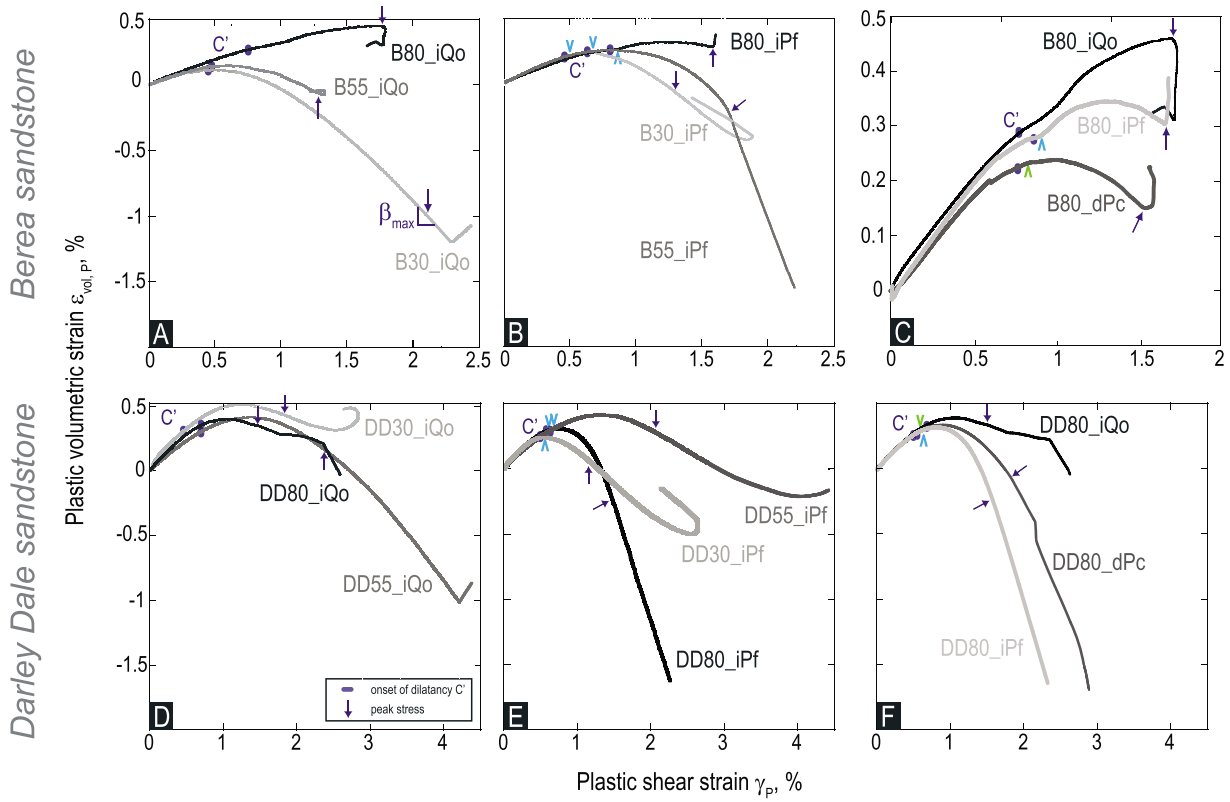

Figure 6. Plastic shear strain γ_P versus plastic volumetric strain $\varepsilon_{vol,P}$ derived from the experimental data of (a, b, and c) Berea and (d, e, and f) Darley Dale sandstone samples deformed at confining pressures of 30, 55, and 80 MPa. Figures 6a and 6d are for the iQo tests; Figures 6b and 6e for the iPf tests. Figures 6c and 6f show the comparison of samples deformed only at $P_c = 80$ MPa. The onset of dilatancy C′ (dark blue short bars) and the peak stress Pks (dark blue arrows) are marked. Beginnings of pore pressure increase and confining pressure decrease are pointed by light blue and green arrowheads, respectively. Dilatancy factor can be calculated as the first derivative of the curve, and the maximum value β_{max} is reached at peak stress.

The critical hardening factor h_{cr} can be calculated using the maximum value of β measured at peak stress and the friction parameter μ in equation (2):

$$\frac{h_{cr}}{G} = \frac{1+\nu}{9(1-\nu)}(\beta-\mu)^2 - \frac{1+\nu}{2}\left(N+\frac{\beta+\mu}{3}\right)^2, \tag{5}$$

where ν is the Poisson ratio, and $N = 1/\sqrt{3}$ for axisymmetric loading [*Rudnicki*, 2004]. The h_{cr}/G values for each test are given in Table 1. All h_{cr} values are negative and the most negative tend to be the ones at low effective pressure.

Wong et al. [1997] show that the hardening modulus h ($=d\tau/d\gamma_p$) for axisymmetric compaction loading is related to the local slope h_{tan} of a stress strain curve in Figure 4:

$$\frac{E}{h} = \frac{\sqrt{3}}{(\sqrt{3}-\mu)}\left(3-\frac{\Delta\varepsilon_{v,P}}{\Delta\varepsilon_{a,P}}\right)\left(\frac{E}{h_{tan}}-1\right), \tag{6}$$

where $E = 2G(1+\nu)$ is the Young's modulus. The theoretical model of *Rudnicki and Rice* [1975] predicts that the hardening modulus $h \le h_{cr}$ is required for shear localization to develop in a dilatant rock. Our microstructural analyses show that shear localization developed in all of the samples (Figure 5), thus the hardening modulus $h \le h_{cr}$. Because h_{cr} values are negative (Table 1), the hardening modulus h must be more negative. Thus, from equation (6) the local slope of the stress strain curve h_{tan} is expected to be negative, i.e., the samples undergo strain softening during failure.

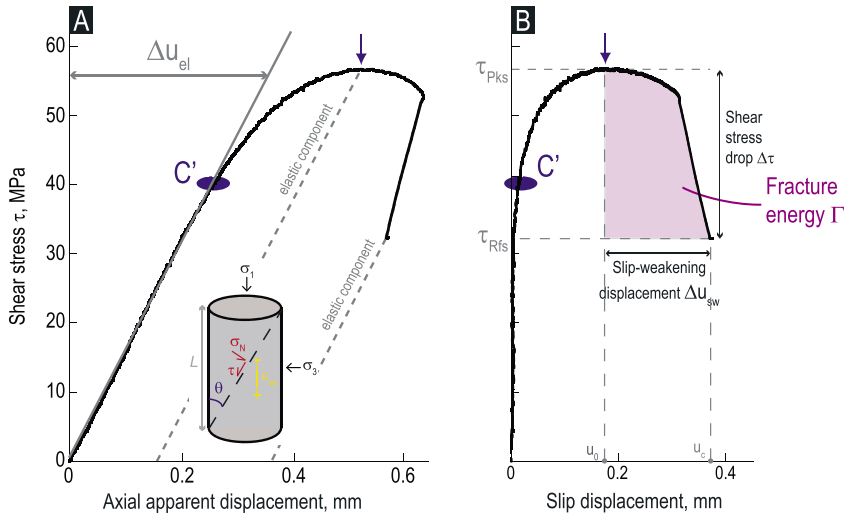

Figure 7. How to calculate slip along a shear fracture in a triaxial deformation test- illustrated with B30_iQo data: shear stress versus (a) axial apparent displacement; (b) slip displacement along the fault plane. The onset of dilatancy *C'* (dark blue short bars) and the peak stress Pks (dark blue arrows) are marked. The gray line in Figure 7a represents quasi-elastic deformation up to *C'*, which is used to calculate the elastic components $\Delta\mu_{el}$ at the peak stress and at the end of the test (dashed lines), respectively. Schematic diagram of a fractured rock sample with initial length of *L* is shown as an insert in Figure 7a. Using the slip weakening model [*Wong*, 1982], axial apparent displacement, effective normal stress σ_N, shear stress τ, and relative slip $\Delta\mu$ along the fault plane can be derived from the axial strain ε_a, differential stress *Q*, and fracture angle θ. With shear stress and relative slip, fracture energy Γ can be obtained (shaded area in Figure 7b).

Previous experimental data show that h_{cr} values maybe unrealistically negative for axisymmetric compression; however, the relative magnitudes of minimum *h* values obtained from porous sandstones undergone shear localization agree with the predicted h_{cr} trend [*Wong et al.*, 1997]. The h_{cr} values calculated from equation (5) can thus provide a quantitative measure of the relative brittleness (i.e., how much strain softening a sample undergoes during failure) among the samples deformed at different conditions, independent of stress drop measurements which are susceptible to uncertainty as the localized rock continues to deform if loading is not terminated.

At low confinements, there is little difference in h_{cr}/G values obtained from iPf and iQo tests, consistent with our observations that the inelastic and failure behaviors are indistinguishable between the different loading configurations in the brittle regime. With increasing effective pressure, the values of h_{cr}/G become less negative. Accordingly, the slope of the stress strain curve after the peak stress is gentler at a higher confining pressure. Sample B80_iQo deformed with constant pore pressure at $P_c = 80$ MPa has the least negative value $h_{cr}/G = -0.17$. In comparison, the h_{cr}/G values for B80_iPf (increasing pore pressure) and B80_dPc (decreasing confining pressure) are -0.28 and -0.31, respectively, considerably different from that of B80_iQo, suggesting enhanced brittleness in these samples (Table 1). The experiments conducted at an intermediate confinement $P_c = 55$ MPa provide a reproducibility measure of the deformation behavior. For Berea sandstone, the hardening and dilatancy parameters show a systematic inelastic and failure behaviors as a function of effective stress. For Darley Dale sandstone, the trend is less clear, likely due to larger sample-to-sample variability.

4.2. Effect of Pore Pressure on Slip Behaviors

A seismic fault can be considered as a shear fracture, and the mechanics of fault slip can be described by brittle fracture propagation using a slip weakening model [*Rice*, 1980]. In such a model, fracture nucleates when shear stress reaches the peak shear strength of a rock. As relative slip increases, shear strength degrades (i.e., slip weakening). At a critical slip distance, frictional sliding occurs for the fracture to propagate. We adapt here the slip weakening model to analyze the slip behavior of rocks during rupture propagation.

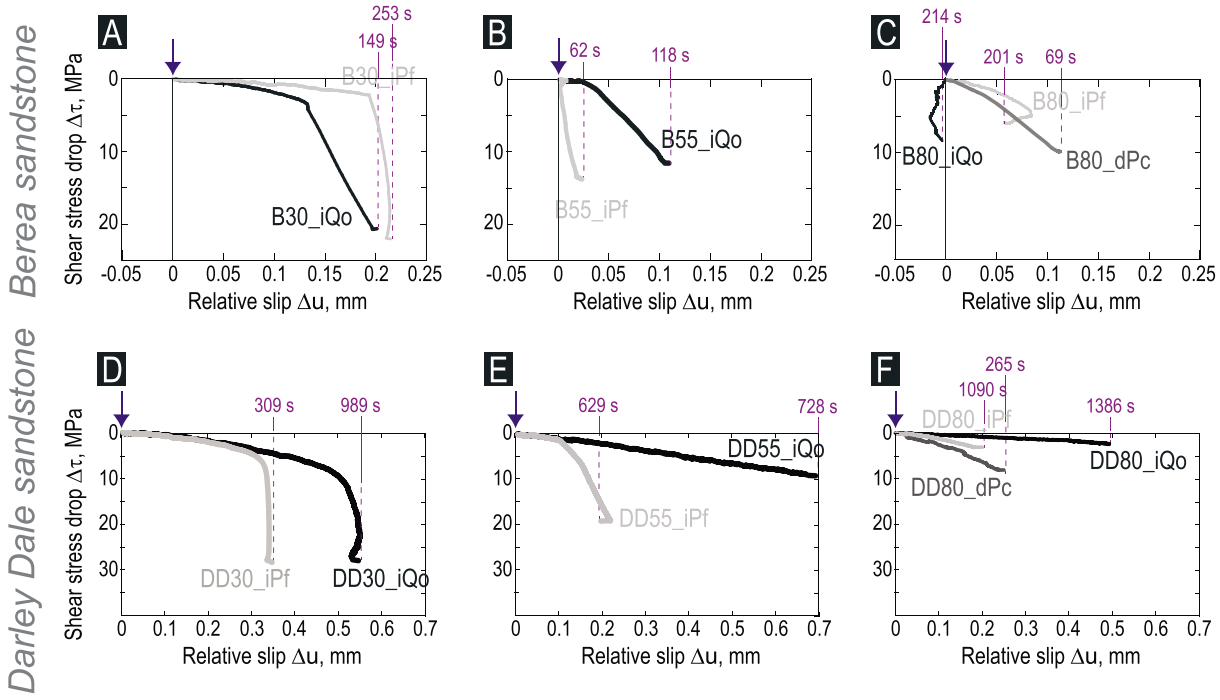

Figure 8. Postpeak stress slip vs shear stress drop of (a, b, and c) Berea and (d, e, and f) Darley Dale sandstones deformed at confining pressures of Figures 8a and 8d 30 MPa, Figures 8b and 8e 55 MPa, and Figures 8c and 8f 80 MPa. Black graphs are for the iQo tests, dark gray graphs for the iPf tests, and light gray graphs for the dPc tests. Relative slip/stress drop durations are given in purple (the time window stops at the first value of residual shear stress).

When a rock fails by brittle faulting, most of the deformation is taken up by slip along the fault plane formed during the postpeak rupture propagation (Figure 5). Following *Wong* [1982] and *Ohnaka et al.* [1997], slip rate associated with faulting can be estimated from the displacement and stress drop recorded (Figure 7).

Defining the fault angle θ as the angle between the σ_1 axis and the macroscopic failure plane (see Figure 7a), the shear stress τ along the failure plane is as follows:

$$\tau = \frac{1}{2}(\sigma_1 - \sigma_3)\sin(2\theta), \tag{7}$$

and apparent slip $\Delta\mu_{app}$ along the fault plane can be expressed in terms of the axial displacement [*Ohnaka et al.*, 1997], providing the knowledge of the axial strain ε_a and the sample length L:

$$\Delta\mu_{app} = \frac{\varepsilon_a L}{\cos\theta}. \tag{8}$$

Note that $\Delta\mu_{app}$ includes the elastic deformation $\Delta\mu_{el}$, as represented by a linear line in Figure 7a, which should be subtracted for evaluating slip along the macroscopic fault plane. Thus, the relative slip $\Delta\mu$ is as follows:

$$\Delta\mu = \Delta\mu_{app} - \Delta\mu_{el} \tag{9}$$

The relative slip $\Delta\mu$ is the integrated amount of slips caused by microcracking as a preparatory phase of imminent macroscopic failure before the peak stress is attained ("slip strengthening"), and slip along the macroscopic failure surface after the peak stress has been attained ("slip weakening") [*Ohnaka et al.*, 1997]. However, as most damage taken by rock samples before peak stress is intragranular cracking throughout the deformed sample with no spatial correlation [e.g., *Lockner et al.*, 1992; see also supporting information Figure S1], which is likely dictated by the distribution of the preexisting defects [*Tamarkin et al.*, 2012], we consider the relative slip only when the shear stress reaches τ_{Pks} (Figure 7b). The shear stress decreases from τ_{Pks} to a constant residual friction stress level τ_{Rfs} as the slip $\Delta\mu$ increases to a critical value μ_c. We estimated τ_{Rfs} as the stable value reached at the end of the stress drop. The displacement $\Delta\mu_{sw}$ is defined by $\Delta\mu_{sw} = \mu_c - \mu_0$

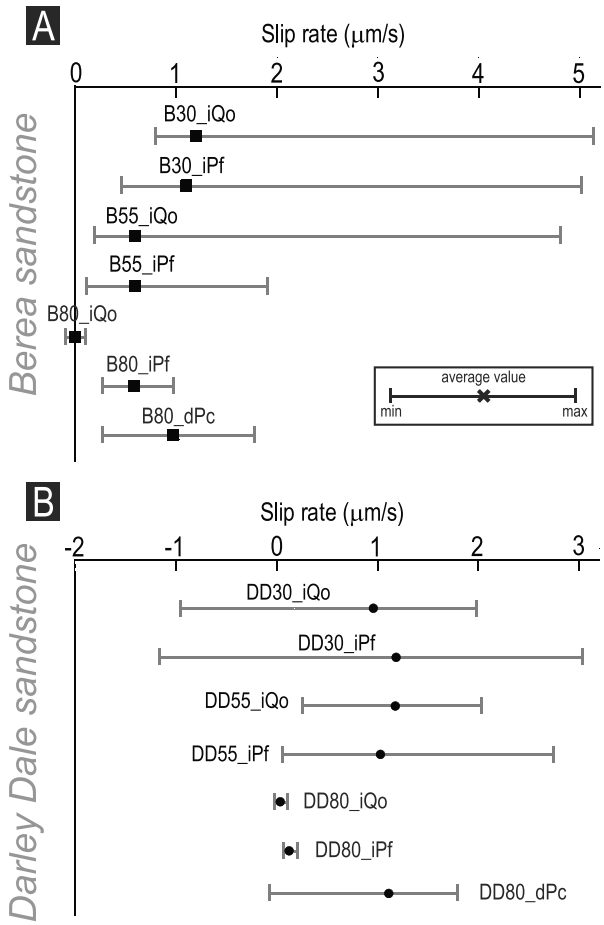

Figure 9. Minimum, average, and maximum slip rate in each test from the data shown in Figure 8.

(with μ_0 being the value of displacement at the peak stress) while $\Delta\tau$ is the breakdown shear stress drop defined by $\Delta\tau = \tau_{Pks}$-τ_{Rfs} (Figure 7b). Within such a framework, the slope of the τ-$\Delta\mu$ curve is always negative.

With increasing effective pressures, both the total shear stress drop and the relative slip decrease during rupture nucleation and propagation (Figure 8), providing a quantitative measure of how increasing pressure prohibit brittle faulting. The shear stress drop $\Delta\tau$ versus relative slip $\Delta\mu$ curves exhibit a characteristic slope change during failure, which marks the onset of frictional sliding along the shear fracture (Figure 8). The slope of the frictional sliding portion of a $\Delta\tau$-$\Delta\mu$ curve during brittle faulting in iPf tests is always steeper in iPf tests compared to that in the iQo tests (minus B80_iQo in which the relative slip is negligible), suggesting that pore pressure buildup enhances slip weakening (Figure 8). Furthermore, the corresponding slope of a dPc test is also slightly steeper than that in an iPf test (Figures 8c and 8f), indicating that decreasing confining pressure is more efficient in augmenting slip weakening. While the overall post failure slip behavior of Darley Dale samples appears more stable compared to Berea samples at the same stress conditions, the relative trends of the effect of pore pressure buildup on slip behavior of the two rocks are in good agreement.

Additional insights on slip rates during failure are gained by plotting the first derivative of the relative slip $\Delta\mu$ versus time *t*, illustrating the instantaneous variation of the slip rate during failure (Figure 9). For Berea samples, it is clear that increasing confining pressure lowers the slip rate (Figure 9a). If pore pressure buildup during deformation does not make a difference to the slip rate in the brittle regime, its influences on slip rate in the transitional regime are twofolds: first, a positive slip rate for B80_iPf compared to the negligible slip rate of B80_iQo; second, the average and maximum values of slip rate of B80_iPf are smaller than those of B80_dPc (and minimum values are equivalent). This slow slip rate of B80_iPf during failure suggests that while the pore pressure buildup enhances brittleness in the transitional regime, the rupture propagation is slower compared to that in the brittle faulting regime (Figure 9a). The slip rates of Darley Dale samples are much slower at the same stress conditions (Figure 9b), suggesting that the slip rate is also a function of intrinsic rock properties.

4.3. Effect of Pore Pressure on Energy Dissipated During Rupture Propagation

Using the criterion derived by *Wong* [1982] from the *J* integral [*Rice*, 1968]—assuming that the breakdown zone size is small relative to the overall fracture size, the shear fracture energy Γ associated with the loss of rock strength during faulting can be calculated as follows:

$$\Gamma = \int_{\mu_0}^{\mu_c} [\tau_{Pks} - \tau_{Rfs}] d\mu. \quad (10)$$

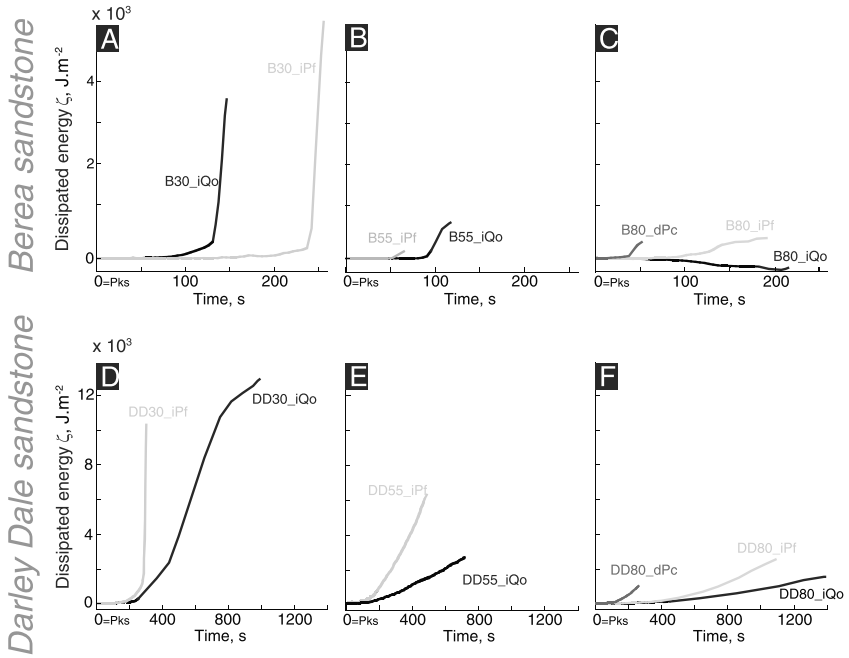

Figure 10. Dissipated energy ζ as function of time during fault nucleation and propagation in (a, b, and c) Berea and (d, e, and f) Darley Dale sandstones deformed at confining pressures of 30 MPa, 55 MPa, and 80 MPa. The maximum value of each curve is the fracture energy Γ.

The area of the purple-shaded portion in Figure 7b is the graphic representation of the shear fracture energy Γ.

The degrading of shear strength is progressive during slip; rapid energy dissipation manifests the fast slip behavior during faulting. To further investigate the rupture propagation process, we calculate the accumulation of dissipated energy ζ at each slip increment $\mu(t)$ and plot ζ as a function of time (Figure 10). After the completion of the stress drop, critical relative slip μ_c is attained and $\zeta = \Gamma$. While the absolute value of Γ critically depends on the pick of μ_c, evolution of $\zeta(t)$ manifests the slowness of rupture propagation.

For the Berea sandstone samples failed in the brittle regime (e.g., $P_c = 30$ and 55 MPa), the sudden increase in slope of $\zeta(t)$ corresponds to the transition from fault nucleation to frictional sliding along the fault (Figures 8a and 8b), and the slope of $\zeta(t)$ decreases with increasing P_c (Figures 10a and 10b). Deformed with increasing pore pressure at the same confinement, the slope of $\zeta(t)$ in B80_iPf is much more gradual during frictional sliding, which is considerably different from that in B30_iQo (Figures 10a and 10c). This shows that the slip behavior of B80_iPf differs from typical dynamic faulting. Interestingly, the slopes of $\zeta(t)$ in B80_iPf and B80_dPc are also different, even though the effective stress states in samples B80_dPc and B80_iPf are nearly identical. These experimental results suggest that not only the value of effective mean stress but also the path taken to reach it affects slip behavior. Compared to Berea sandstone samples deformed at the same confinements, the slope of $\zeta(t)$ in Darley Dale samples are overall more gradual (Figures 10d–10f), suggesting that the rupture propagation in Darley Dale samples is slower. Notwithstanding these differences, in both rocks, the slope of $\zeta(t)$ increases in the iPf tests compared to that in the corresponding iQo tests when the overall slip rate is slow. Our interpretation is that pore pressure buildup during deformation enhances slip instability, but the effect may not be measurable if the slip rate is fast. It seems also likely to observe a spectrum of different slip behaviors in different rocks even when subjected to the same tectonic settings.

We examine the scaling relation between ζ and slip duration in our deformation experiments. The slope of $\log(\zeta)$ versus $\log(t)$ during rupture propagation is plotted in Figure 11. In general, the slope increases with increasing confinements and decreases with increasing pore fluid pressure or decreasing confining pressure even if the difference may be slight (Figure 11). Berea samples deformed in the brittle regime have low slopes ranging between 0.02 and 0.07 (Figure 11a), indicating fast energy dissipation during rupture propagation.

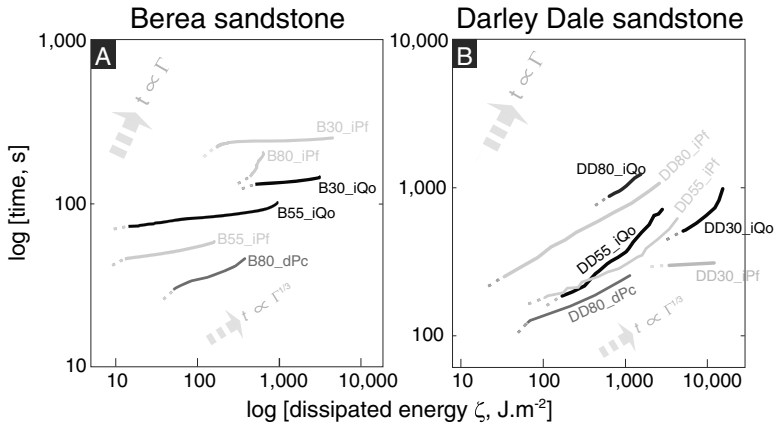

Figure 11. Log-log plot of time versus dissipated energy ζ during fault nucleation and propagation in all (a) Berea and (b) Darley Dale sandstones deformed at confining pressures of 30 MPa (light gray), 55 MPa (dark gray), and 80 MPa (black), respectively. For reference, the linear dependence of slow slip phenomena as calculated by *Ide et al.* [2007] and cubic law of regular earthquakes are illustrated in gray thick arrows.

While no slip was detected in B80_iQo, the slope of B80_iPf with increasing pore pressure is 0.7. This value is 1 order of magnitude higher compared to those in B30 and B55 samples (Figure 11a), indicating much slower energy dissipation. In comparison, the slope of B80_dPc with decreasing confining pressure is ~0.1, indicating a faster energy dissipation and closer to that in samples deformed in the brittle regime. Darley Dale samples failed in the brittle regime have slopes ranging between 0.4 and 0.6 (Figure 11b), comparable to that of B80_iPf, implying similar slowness. At iPf conditions, DD30_iPf sample has a slope of ~0.03, within the range of 0.02–0.07 for Berea samples failed in the brittle regime, suggesting that pore pressure buildup could enhance slip in the brittle regime. The lack of detectable differences in slopes of Berea samples deformed at iPf conditions under low confinements could be due to the limitation of the data acquisition, i.e., the rupture propagation could be too fast to be recorded.

The relationship between log(ζ) and log(t) in the transition regime has different character compared to that of brittle faulting. While the experimental conditions were such that a millimeter scale slip event occurs during fault propagation, the postfailure process consists of numerous microcracking events, with the duration of each event lasting a fraction of a second. The near constant slope of log(ζ) versus log(t) implies no change in scaling relation between the microevents and the main centimeter scale slip event. However, compared to the Berea sandstone samples, there are more variations between the Darley Dale samples. Further experiments are needed to elucidate the relationship of shear fracture energy and faulting process.

Ide et al. [2007] proposed that slow slip events follow a unified scaling law in which moment scales linearly with duration. In contrast, moments for ordinary earthquakes are known to scale as duration cubed. The difference in log(ζ) versus log(t) relationship between brittle faulting and pore pressure enhanced instability resembles the differences observed in seismic events (Figure 11). Because the energy dissipated during rupture propagation in deformation experiments and the seismic moments recorded during earthquakes are both brittle failure processes, our data may shed light on the current discussion on the moment-duration relationship in seismic studies [e.g., *Ide et al.*, 2007; *Peng and Gomberg,* 2010]. If laboratory deformation experiments bear some relevance to faulting mechanics in the field, our data suggest that (1) slip rate and energy budget during rupture propagation may vary at different tectonic settings; (2) excess pore pressure enhances slip and is responsible for inducing slow slip behavior along a creeping fault; and (3) the slip behaviors during faulting can vary considerably even in slightly different rocks, although all the other conditions (pressure, temperature, interstitial fluids, etc.) are the same. This would imply that fault rupture in nature could generate different slip behaviors at different tectonic settings.

4.4. Micromechanisms of Rupture Propagation in Porous Rocks

Grain scale frictional sliding and Hertzian cracking are dominant micromechanisms that control the brittle-ductile transition in porous sandstones [*Wong et al.*, 1997]. The relatively simple micromechanics associated with the brittle-ductile transition in porous sandstones [e.g., *Wong et al.*, 1997] lead to straightforward

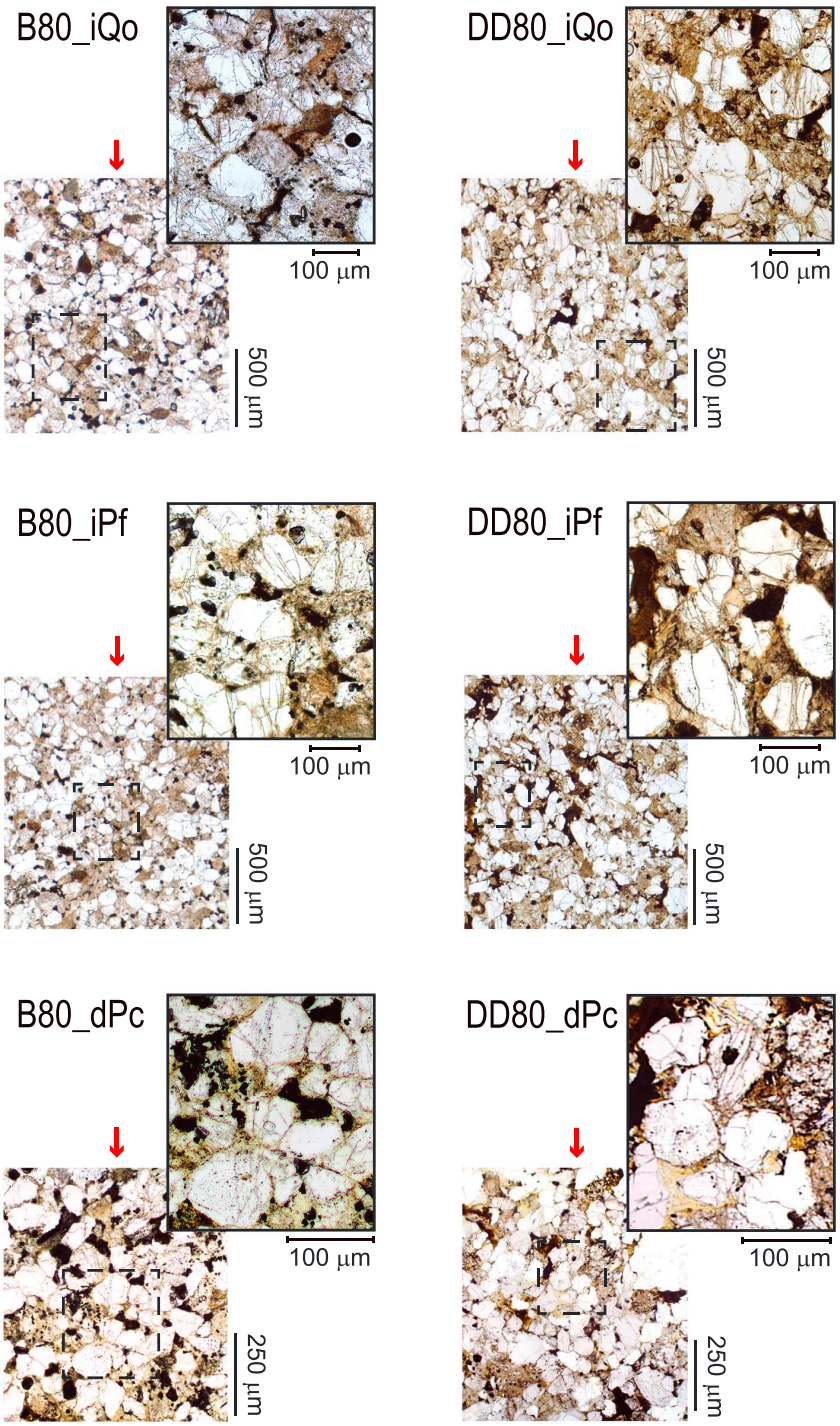

Figure 12. Micrographs of six deformed samples at $P_c = 80$ MPa. (top) Berea samples B80_iQo, B80_iPf and B80_dPc; (bottom) Darley Dale samples D80_iQo, D80_iPf and D80_dPc. Dashed boxes mark the regions within a localized shear band where high-resolution images are shown as inserts. Grain crushing is observed within the shear band, and microcracks form preferentially along to the maximum principal stress σ_1 direction (red arrow).

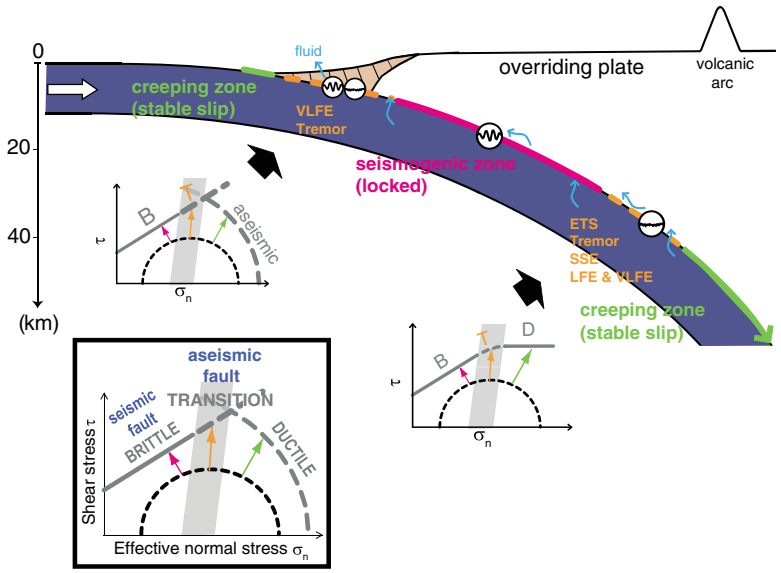

Figure 13. Spectrum of slip behaviors and mechanical regime of deformation associated in subduction zone context. Solid green lines illustrate the stable creeping zones where rocks are assumed to deform aseismically in granular or ductile flow; dashed orange lines point out the updip and downdip transitional zones of deformation; heavy solid magenta line indicates the extent of coseismic slip where rocks deformed in the brittle regime producing earthquakes. Failure modes in each zone are illustrated by the Mohr's diagrams.

comparison of slip behaviors in different regimes, with or without decreasing effective pressure. Intensive microcracking marks the microscale damage in all samples. The macroscopic fault developed along zones of intensive damage (Figure 5). Under compressive loading and at high confinement, dilatancy hardening resulting from crack growth (i.e., dilatancy-induced suction in a fluid-saturated rock caused by cracking) impedes rupture propagation in saturated, drained rocks [*Rudnicki and Chen*, 1988].

Figure 12 shows a preferential crack orientation subparallel to maximum principal stress σ_1 in all deformed samples. In B80_iQo, multiple intragranular cracks partially transecting grains are observed. In B80_dPc, we see less intragranular cracks only partially transecting grains. However, in B80_iPf, most cracks transect the whole grains, with many developed across several grains. Our interpretation is that, at a given time, the constant pore pressure at the crack tips could not be maintained and effective mean stress locally increased, thus delaying the microcrack propagation [e.g., *Rudnicki and Chen*, 1988]. This indicates a dilatancy hardening effect during the rupture process. The more the underlying drained condition could not be satisfied at a given time during the ongoing deformation, the more intragranular cracks formed. Increasing pore pressure, however, facilitates crack propagation as it sufficiently compensates the suction effect induced by dilation (i.e., dilatancy hardening). In Darley Dale samples deformed at $P_c = 80$ MPa, cracks are mostly transgranular (transecting the whole grains) which is consistent with the brittle failure mode of deformation of those samples. And there are also more intergranular cracks (i.e., cracks can be traced across several grains) in DD80_iPf than those in DD80_iQo, suggesting again enhanced crack propagation by increasing pore fluid pressure.

We note that the maximum overpressure needed to overcome the dilatancy hardening in this experiment was $P_f \sim 18$ MPa (Figures 4 and 5 and Table 1), so well below the lithostatic pore pressure condition. The differences in microscale damage distribution and localization observed between the two sandstones show why slip behaviors during faulting vary considerably in different rocks, even if all the other conditions (pressure, temperature, interstitial fluids, etc.) are the same.

4.5. Relevance to Earthquake Faulting

Using porous sandstones, our experimental results confirm the existence of transient slip behavior between the dynamic slip and the continuous creep. Our study brings constraints on how the interplay between dynamic rupture and stable localized damage produces slow slip events in porous rocks. The slowness of

rupture propagation varies considerably among different rocks. Environmental conditions, such as pressure, temperature, strain rate, and interstitial fluid, exert important control on slip rate. In the transitional regime where dynamic faulting is prohibited, increasing pore fluid pressure can induce slow slip. In porous rocks, the deformation mechanism that controls such slip behavior is the interaction between unstable crack growth and dilatancy hardening [e.g., *Rudnicki and Chen*, 1988].

Our experimental results suggest that increasing pore pressure induces slow slip only when failure is in the transitional regime; pore pressure buildup in the brittle regime enhances the brittleness and slip rate. This implies that slow slip phenomena take place in regions where rocks have undergone the brittle-ductile transition, which is in good agreement with recent observations of the close proximity between slow slip phenomenon and the transitional zones, such as the base of the seismogenic layer [e.g., *Nadeau and Dolenc*, 2005].

Slow slip phenomena are observed in both the updip and downdip limits (orange zones in Figure 13) at the subduction regions. While the seismic-aseismic transition at the updip is controlled by the consolidation state and mineralogy of the subducting sediments and high pore pressure generation is due to compaction and clay dehydration [*Saffer and Tobin*, 2011], the downdip region transition is likely controlled by enhanced plasticity and metamorphic dehydration reactions that are sensitive to higher temperatures [*Peacock*, 2011]. Despite the differences in deformation mechanisms, as shown in the Mohr's diagrams in Figure 13, failure modes at both updip and downdip limits (marked in orange) are in the brittle-ductile transition regime. Given the petrological and seismic evidence of excess pore pressure at the updip [e.g., *Saffer and Tobin*, 2011] and downdip [e.g., *Shelly et al.*, 2006] limits, it is not surprising that slow slip events are detected in these regions [e.g., *Obana and Kodaira*, 2009; *Obara*, 2002].

Most source physics models focus on inhibiting seismic faulting to generate slow slip [e.g., *Segall et al.*, 2010]. However, it has been observed along the Pacific subduction zone that the regions with the greatest aseismic slip do not spatially correspond to the regions of greatest tremor. In Cascadia, Alaska, Mexico, and some parts of Japan, the tremor is at the downdip edge of the aseismically slipping zone (J. Gomberg, personal communication, 2014). In the light of our experimental data we propose that these tremor activities could result from enhanced aseismic slip, instead of impeded seismic slip.

As illustrated in the Mohr's diagrams, although deformation mechanisms may vary in different tectonic settings, failure mode at the locked region (in pink in Figure 13) is in the brittle regime, it is unlikely for slow slip events to take place in the locked region even if pore pressure buildup occurs. High pore pressure will primarily reduce the shear strength and cause enhanced seismicity in this region. Below the downdip limits (in green in Figure 13), failure mode, as shown in the bottom Mohr's diagram, is ductile flow. Because deformation mechanisms are dominantly pressure-insensitive plastic flow in this region, the influence of increasing pore pressure on slip instability diminishes [*Thomas et al.*, 2012]. Consequently, slow slips are not likely to occur.

Finally, our data show that many factors, such as lithology and increasing pore pressure, could affect slip behaviors. While pore pressure buildup in the transitional regime induced slow slips, near lithostatic pore pressure is not always necessary. Because generation and maintenance of near lithostatic pressure in an active tectonic region is difficult [*Peacock*, 2011], the lesser overpressure requirement is in a better agreement with the prevalence of the slow slip phenomena.

5. Conclusions

We report triaxial deformation experiments that provide evidence on how pore fluid pressure buildup during failure affects slip behavior and rupture propagation. We used three loading configurations to compare the inelastic behavior and failure modes of two sandstone samples deformed under increasing pore pressure (iPf tests), constant pore pressure (iQo tests), or decreasing confining pressure (dPc tests), respectively. Our results indicate that in the brittle regime, increasing pore pressure reduces rock's brittle strength but does not induce different slip behavior. However, in the transitional regime where dynamic faulting is prohibited, pore pressure buildup during failure enhances localization and the slip behavior is distinctively different from that during dynamic faulting. Using the existing theoretical framework, we quantified the effect of excess pore pressure on fault nucleation and propagation. Slip rate and shear fracture energy were calculated for each sample during faulting. Finally, our data suggest that different slip behaviors should be expected in rocks deformed at similar effective stresses as it will depend on loading paths.

Acknowledgments
This project is supported by the National Science Foundation through a CAREER grant NSF-EAR1056317 and the Department of Energy through grant DE-FG02-07ER15916. We thank D. Lockner and P. Meredith for providing the sandstone samples. Technical support Thomas Tamarkin and Ted Koczynski are gratefully acknowledged. We thank Sarah Penniston-Dorland for her assistance in the optical microscopy lab. We thank Joan Gomberg for discussion, review of the draft, and her suggestions. We are grateful to Nicola De Paola, Diane Moore, and John Rudnicki for their constructive comments and suggestions that greatly improved the presentation of the manuscript. Data from this study are available upon request from the authors.

References

Andrews, D. J. (2002), A fault constitutive relation accounting for thermal pressurization of pore fluid, *J. Geophys. Res.*, *107*(B12), 2363, doi:10.1029/2002JB001942

Baud, P., E. Klein, and T.-F. Wong (2004), Compaction localization in porous sandstones: Spatial evolution of damage and acoustic emission activity, *J. Struct. Geol.*, *26*, 603–624.

Byerlee, J. (1968), Brittle-ductile transition in rocks, *J. Geophys. Res.*, *73*, 4741–4750, doi:10.1029/JB073i014p04741.

De Paola, N., D. R. Faulkner and C. Collettini (2009), Brittle versus ductile deformation as the main control on the transport properties of low-porosity anhydrite rocks, *J. Geophys. Res.*, *114*, B06211, doi:10.1029/2008JB005967.

De Paola, N., T. Hirose, T. Mitchell, G. Di Toro, C. Viti, and T. Shimamoto (2011), Fault lubrication and earthquake propagation in thermally unstable rocks, *Geology*, *39*, 35–38, doi:10.1130/G31398.1.

Fisher, Q. J., S. D. Harris, M. Casey, and R. J. Knipe (2007), Influence of grain size and geothermal gradient on the ductile-to-brittle transition in arenaceous sedimentary rocks: implications for fault structure and fluid flow, *Geol. Soc. London Spec. Publ.*, *289*, 105–121, doi:10.1144/SP289.7.

Foster, J. H., A. R. Lowry, and B. A. Brooks (2013), Fault frictional parameters and material properties revealed by slow slip events at Kilauea volcano, Hawaii, *Geophys. Res. Lett.*, *40*, 6059–6063, doi:10.1002/2013GL058234.

Healy, J. H., W. W. Rubey, D. T. Griggs, and C. B. Raleigh (1968), The Denver earthquakes, *Science*, *161*, 1301–1310, doi:10.1126/science.161.3848.1301.

Ide, S., D. Shelly, and G. Beroza (2007), Mechanism of deep low frequency earthquakes: Further evidence that deep non-volcanic tremor is generated by shear slip on the plate interface, *Geophys. Res. Lett.*, *34*, L03308, doi:10.1029/2006GL028890.

Jaeger, J. C., N. G. W. Cook, and R. Zimmerman (2007), *Fundamentals of Rock Mechanics*, 4th ed., Wiley-Blackwell, Oxford, U. K.

Keranen, K. M., M. Weingarten, G. A. Abers, B. A. Bekins, and S. Ge (2014), Sharp increase in central Oklahoma seismicity since 2008 induced by massive wastewater injection, *Science*, *345*, 448–451, doi:10.1126/science.1255802.

Kitajima, H., and D. Saffer (2012), Elevated pore pressure and anomalously low stress in regions of low frequency earthquakes along the Nankai Trough subduction megathrust, *Geophys. Res. Lett.*, *39*, L23301, doi:10.1029/2012GL053793.

Lachenbruch, A. H. (1980), Frictional heating, fluid pressure, and the resistance to fault motion, *J. Geophys. Res.*, *85*(B11), 6097–6112, doi:10.1029/JB085iB11p06097.

Lockner, D. A., J. D. Byerlee, V. Kuksenko, A. Ponomarev, and A. Sidorin (1992), Observations of quasistatic fault growth from acoustic emissions, in *Fault Mechanics and Transport Properties of Rocks: A Festschrift in Honor of W. F. Brace*, edited by B. Evans and T.-F. Wong, Academic Press, London.

Makhnenko, R. Y., and J. F. Labuz (2015), Dilatant hardening of fluid-saturated sandstone, *J. Geophys. Res. Solid Earth*, *120*, 909–922, doi:10.1002/2014JB011287.

Menendez, B., W. Zhu, and T.-F. Wong (1996), Micromechanics of brittle faulting and cataclastic flow in Berea sandstone, *J. Struct. Geol.*, *18*, 1–16.

Murrell, S. A. F. (1977), Natural faulting and the mechanics of brittle shear failure, *J. Geol. Soc. Lond.*, *133*, 175–189.

Nadeau, R., and D. Dolenc (2005), Nonvolcanic tremors deep beneath the San Andreas fault, *Science*, *307*, doi:10.1126/science.1107142.

Obana, K., and S. Kodaira (2009), Low-frequency tremors associated with reverse faults in a shallow accretionary prism, *Earth Planet. Sci. Lett.*, *287*, 168–174.

Obara, K. (2002), Nonvolcanic deep tremor associated with subduction in southwest Japan, *Science*, *296*, 1679–1681.

Ohnaka, M., M. Akatsu, H. Mochizuki, A. Odedra, F. Tagashira, and Y. Yamamoto (1997), A constitutive law for the shear failure of rock under lithospheric conditions, *Tectonophysics*, *277*, 1–27.

Ougier-Simonin, A., and W. Zhu (2013), Effects of pore fluid pressure on slip behaviors: An experimental study, *Geophys. Res. Lett.*, *40*, 2619–2624, doi:10.1002/grl.50543.

Paterson, M., and T. Wong (2005), *Experimental Rock Deformation—The Brittle Field*, Springer, Berlin.

Peacock, S. M. (2011), High pore pressures and porosity at 35 km depth in the Cascadia subduction zone, *Geology*, *39*, 471–474, doi:10.1130/G31649.1.

Peng, Z., and J. Gomberg (2010), An integrated perspective of the continuum between earthquakes and slow-slip phenomena, *Nat. Geosci.*, *3*, 599–607, doi:10.1038/NGEO940.

Platt, J. D., J. W. Rudnicki, and J. R. Rice (2014), Stability and localization of rapid shear in fluid-saturated fault gouge, 2. Localized zone width and strength evolution, *J. Geophys. Res. Solid Earth*, *119*, 4334–4359, doi:10.1002/2013JB010711.

Read, M., M. Ayling, P. Meredith, and S. Murrell (1995), Microcracking during triaxial deformation of porous rocks monitored by changes in rock physical properties, II. Pore volumometry and acoustic emission measurements on water-saturated rocks, *Tectonophysics*, *245*, 223–235.

Rice, J. (1968), A path independent integral and the approximate analysis of strain concentration by notches and cracks, *J. Appl. Mech.*, *35*, 379–386.

Rice, J. (1975), On the stability of dilatant hardening for saturated rock masses, *J. Geophys. Res.*, *80*, 1531–1536, doi:10.1029/JB080i011p01531.

Rice, J. (1980), The mechanics of earthquake rupture, in *Physics of the Earth's Interior*, edited by A. Dziewonski and E. Boschi, pp. 555–649, North Holland Publishing Company, Amsterdam.

Rice, J., and M. P. Cleary (1976), Some basic stress diffusion solutions for fluid saturated elastic porous media with compressible constituents, *Rev. Geophys.*, *14*, 227–241, doi:10.1029/RG014i002p00227.

Rudnicki, J., and C.-H. Chen (1988), Stabilization of rapid frictional slip on a weakening fault by dilatant hardening, *J. Geophys. Res.*, *93*(B5), 4745–4757, doi:10.1029/JB093iB05p04745.

Rudnicki, J., and J. Rice (1975), Conditions for the localization of deformation in pressure-sensitive dilatant material, *J. Mech. Phys. Solid.*, *23*, 371–394.

Rudnicki, J. W. (2004), Shear and compaction band formation on an elliptic yield cap, *J. Geophys. Res.*, *109*, B03402, doi:10.1029/2003JB002633.

Saffer, D., and H. Tobin (2011), Hydrogeology and mechanics of subduction zone forearcs: Fluid flow and pore pressure, *Annu. Rev. Earth Planet. Sci.*, *39*, 157–186.

Scholz, C. (2002), *The Mechanics of Earthquakes and Faulting*, 2nd ed., Cambridge Univ. Press, U. K.

Segall, P., A. M. Rubin, A. M. Bradley, and J. R. Rice (2010), Dilatant strengthening as a mechanism for slow slip events, *J. Geophys. Res.*, *115*, B12305, doi:10.1029/2010JB007449.

Shelly, D., G. Beroza, S. Ide, and S. Nakamula (2006), Low-frequency earthquakes in Shikoku, Japan, and their relationship to episodic tremor and slip, *Nature*, *442*, 188–191.

Sibson, R. H. (1973), Interactions between temperature and pore fluid pressure during earthquake faulting: A mechanism for partial or total stress relief, *Nat. Phys. Sci.*, *243*, 66–68.

Sibson, R. H. (1986), Earthquakes and rock deformation in crustal fault zones, *Annu. Rev. Earth Planet. Sci.*, *14*, 149–175, doi:10.1146/annurev.ea.14.050186.001053.

Sibson, R. H. (2003), Thickness of the seismic slip zone, *Bull. Seismol. Soc. Am.*, *93*, 1169–1178, doi:10.1785/0120020061.

Tamarkin, T., A. Ougier-Simonin, and W. Zhu (2012), Progressive microscopic damage associated with fault growth, *Geophys. Res. Lett.*, *39*, L15303, doi:10.1029/2012GL052487.

Thomas, A. M., R. Bürgmann, D. R. Shelly, N. M. Beeler, and M. L. Rudolph (2012), Tidal triggering of low frequency earthquakes near Parkfield, California: Implications for fault mechanics within the brittle-ductile transition, *J. Geophys. Res.*, *117*, B05301, doi:10.1029/2011JB009036.

Wong, T.-F. (1982), Shear fracture energy of Westerly granite from post-failure behavior, *J. Geophys. Res.*, *87*, 990–1000, doi:10.1029/JB087iB02p00990.

Wong, T.-F., C. David, and W. Zhu (1997), The transition from brittle faulting to cataclastic flow in porous sandstone: Mechanical deformation, *J. Geophys. Res.*, *102*, 3009–3025, doi:10.1029/96JB03281.

Zhu, W., and T.-F. Wong (1997), The transition from brittle faulting to cataclastic flow: Permeability evolution, *J. Geophys. Res.*, *102*, 3027–3041, doi:10.1029/96JB03282.